Journal of Zhejiang University-SCIENCE A (Applied Physics & Engineering) 2024 25(7):596-604
www.jzus.zju.edu.cn; www.springer.com/journal/11582
E-mail: jzus_a@zju.edu.cn

Correspondence

https://doi.org/10.1631/jzus.A2300479

Check for updates

Novel soft robotic finger model driven by electrohydrodynamic (EHD) pump

Xuehang BAI[1*], Yanhong PENG[2*], Dongze LI[3], Zhuochao LIU[4], Zebing MAO[5✉]

[1]*Department of Mechanical, Automotive and Materials Engineering, Faculty of Engineering, University of Windsor, Windsor N9B 3P4, Canada*
[2]*Department of Information and Communication Engineering, Graduate School of Engineering, Nagoya University, Nagoya 464-8601, Japan*
[3]*Department of Intelligent Science and Technology, College of Computer Science and Technology, Qingdao University, Qingdao 266071, China*
[4]*Design and Research Institute of University of Science and Technology Beijing Co. Ltd., Beijing 100083, China*
[5]*Faculty of Engineering, Yamaguchi University, Yamaguchi 755-8611, Japan*

1 Introduction

In the field of robotic-human interactions, soft robotics offers enhanced safety and adaptability. A major challenge in this area is the integration of soft actuators with pump systems, which often increases the system volume and complexity. This study presents the development and testing of a robotic finger powered by electrohydrodynamic (EHD) pumps. By leveraging the electric field-induced flow of dielectric fluids, the robotic finger incorporates a flexible rubber sheet embedded with purely soft EHD pumps, causing the deflection of polypropylene (PP) sheet. Upon voltage application, the pumps induce controlled bending motion in the robotic finger, achieving a maximum bending angle of 37° with a 10 kV input constant direct current voltage. A comprehensive mathematical model is presented to bridge the gap between the EHD pump system and finger dynamics, which accurately describes the entire system from the EHD driving mechanism to the mechanical actions of the robot. Experiments are conducted to validate this model, which reveal a strong correlation between the input voltage to the EHD pump and the resultant bending angle of the robotic finger. The innovations of this study not only provide insights into the integration of EHD pumps with soft robotics but also introduce a novel modeling approach that can guide future work in EHD pump-robot systems.

Soft robotics is a rapidly burgeoning field dedicated to the design and development of robots capable of safe and adaptable interactions with human beings and their surroundings. These robots are constructed from soft, flexible, and compliant materials, with the aim to replicate the motion and behavior observed in natural organisms (Peng et al., 2022; Zhang et al., 2023). Mainly driven by EHD pumps possessing flexible, stretchable, modular, scalable, quiet, and fast response characteristics (Cacucciolo et al., 2019), soft robots can integrate pneumatic (Funabora, 2018; Kobayashi et al., 2022), hydraulic (Mao et al., 2019b, 2022a), and dielectric driving sources (Tan et al., 2022). The control strategies of these robots have also evolved to a certain extent. For instance, Chen et al. (2022) optimized the structural design of a dielectric elastomer finger used in low-force robotic grippers to mimic the human thumb profile. Peng et al. (2023a) reported on the creation and assessment of a wearable assistive device inspired by human muscle configuration and a soft robot resembling a large intestine, which uses pneumatic McKibben muscles (Peng et al., 2024). Jiao et al. (2021) integrated re-foldable origami into soft-matter artificial muscles, which enable versatile multimode morphing with complex compound motions. Kong et al. (2024) proposed self-propelled swimmers using ultrasonic transducers. Tawk et al. (2021) implemented a cost-effective and open-source 3D printing process to develop a 3D-printed soft monolithic robotic finger with embedded soft pneumatic sensing

✉ Zebing MAO, mao.z.aa@yamaguchi-u.ac.jp
* The two authors contributed equally to this work
Zebing MAO, https://orcid.org/0000-0002-2944-7151

Received Sept. 20, 2023; Revision accepted Dec. 18, 2023;
Crosschecked Mar. 21, 2024; Online first Apr. 25, 2024

chambers for position and touch sensing. Shen et al. (2023) devised a data-driven control approach for soft robotics enabling the robot to undergo significant morphological changes. However, none of these soft finger actuators can be seamlessly integrated into the internal structure of the pump, necessitating the allocation of an extra space to accommodate these materials and actuators. This integration challenge not only increases the overall volume and complexity of the pump system but also may lead to mechanical connectivity issues and potential leakage risks due to the need to connecting these materials with other components of the pump system. An EHD pump can leverage the electric field-induced flow of dielectric fluids, instigate the motion and deformation of soft actuators (Nagaoka et al., 2019; Mao et al., 2020b, 2021), and generate droplets (Mao et al., 2019a, 2019b, 2020c). EHD pump-driven actuators possess distinct advantages compared to their traditional counterparts, including a flexible body, noiseless operation, and the lack of mechanical wear (Peng et al., 2023b). Numerous studies have focused on the modeling and actuation of EHD pump due to its excellent mechanical properties. For example, Mao et al. (2020b) integrated an EHD jet generator into a soft fiber-reinforced tube, addressing the challenge posed by bulky power sources in fluidic elastomer actuators employed in soft robotics. This innovative application of EHD dynamics permits power source miniaturization and offers potential advancements for EHD-based soft robots. Moreover, Smith et al. (2023) integrated pressure fluid circuits into textiles, allowing for muscle support, thermal regulation, and tactile feedback in a portable, wearable form. Nevertheless, the above studies predominantly focus on modeling the power source process rather than develop a comprehensive mathematical model encompassing the entire system. To this end, Mao et al. (2023) improved the prediction of critical heat flux for flexible EHD pumps using machine learning algorithms. By optimizing the input parameters and adopting the best predictive model, they achieved high accuracy in predicting pressure and flow, offering valuable insights into the design of fluid sources in flexible soft actuators and hydraulic sources of microfluidic chips. The deep learning model can achieve high accuracy; however, it remains a ‘black box’ and thus it lacks the ability to provide explanations for its predictions.

This paper introduces an EHD robotic finger and a mathematical model of the power source and robot actuation. This marks the first instance of constructing an integrated robotic finger that incorporates a flexible elastomer rubber sheet embedded with stacked, purely soft EHD pumps. These pumps are actuated by a working fluid upon the application of voltage, resulting in controlled bending motion. Owing to the applied high voltage transformer regulation and controller regulation, the robotic finger can achieve a maximum bending angle of 37° under an input voltage of 10 kV. Unlike previous studies that mainly rely on experimental or simulation verification (Nagaoka et al., 2019; Mao et al., 2020b), this study develops a mathematical model to explore the relationship between the input voltage applied to the EHD pump and the resulting bending angle of the robotic finger. The model elucidates the connection between these two systems—the EHD source and the robot linkage mechanism—and demonstrates consistency with the experimental results. The contributions of this study lie in the development of a soft EHD pump-driven robotic finger and a comprehensive mathematical model that features the entirety of the EHD driving system and the robot mechanical system. Validation is performed through experimentation involving extension and flexion, which indicates the potential of this model to inspire novel approaches in mapping other EHD pump-robot action systems.

2 Method

This study investigates the performance of an EHD robotic finger joint through an experimental design. First, the robotic finger joint is successfully manufactured, then experiments of fulfilling the bending function are conducted on the structure. Meanwhile, the angle of bending and the voltage of electrification are recorded as raw data. Finally, the relationship between two variables is determined and analyzed.

2.1 Structure

The robotic finger joint comprises of three main components, namely, EHD pumps, a one-layer actuator, and a control circuit (Fig. 1). To ensure the energy efficiency and reliability of the system during operation, we utilized a low-power EHD pump with layered structure (Fig. 1a). In our previous work, we

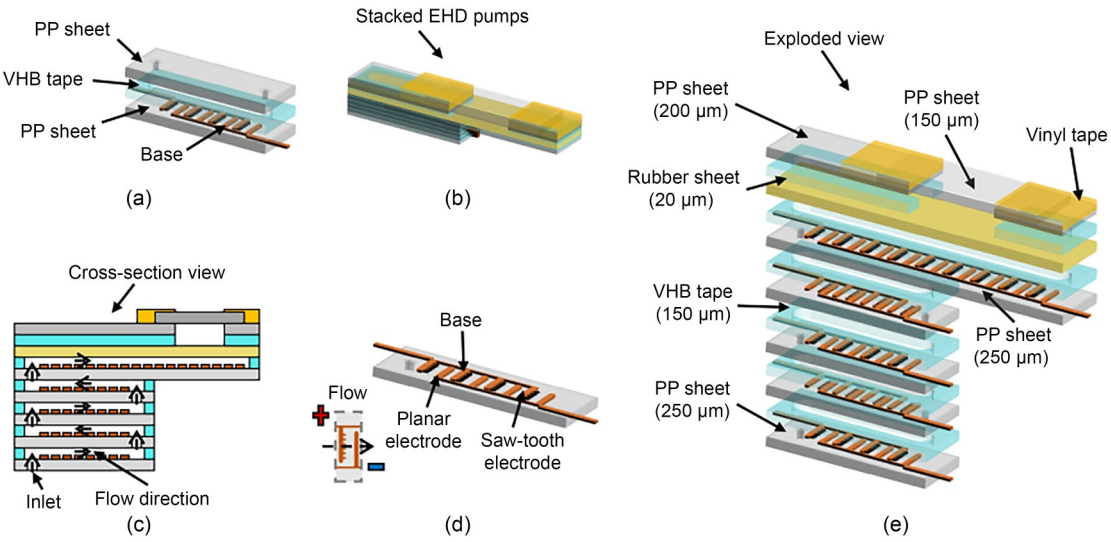

Fig. 1 Stacked EHD pump structure and breakdown of a single EHD pump: (a) layered construction of a single EHD pump; (b) stacking configuration of EHD pumps; (c) illustration of electrolyte flow direction; (d) electrode design; (e) exploded view of stacked EHD pumps and finger actuators. VHB: very high bonding

demonstrated that a singular pump layer is capable of generating a maximum pressure of approximately 3.2 kPa. With the incorporation of four pump layers, the attainable maximum pressure escalates to 12.8 kPa. In addition, the solitary one-layer actuator can independently produce an approximate pressure of 10 kPa. As a result, the cumulative impact of the four-layer pump configuration and the one-layer actuator results in a combined pressure of approximately 22 kPa. This value is deemed adequate for facilitating effective device deflection to explore angular relationships in this work. Four stacked mini EHD pumps (Fig. 1b), which can also reduce manufacturing complexity and enhance the integration of the robotic finger joint, are interconnected end-to-end, creating an S-shaped channel for electrolyte flow (Fig. 1c). A previous study (Darabi et al., 2002) showcased that electrodes designed with a saw-tooth configuration can generate high flow rates and pressure. We have incorporated this design, with each layer of the EHD pump consisting of four pairs of electrodes configured in a saw-tooth pattern (Fig. 1d). The breakdown voltage for the electrodes is 16 kV. The actuator is an elongated iteration of the EHD pump, featuring nine electrode pairs that enhance power generation while serving as a structural support for the finger component. Fig. 1e illustrates the entire configuration of the robotic finger joint, which comprises of stacked EHD pumps and actuator. The actuator includes a pump structure constructed from a PP sheet at its base, with the electrolyte flow sandwiched between the pump and a central rubber sheet. The connection point between the thin, hollow PP sheet and the rubber sheet is positioned directly above the latter to maintain a minimal gap for an optimized application of force by the rubber sheet. It is essential to note that the material strength of the PP used in this structure is 30 MPa, indicating its capacity to withstand up to 30 MPa of stress per unit area before deformation or failure. The actuator receives electrolyte fluid from pumps and uses it to generate substantial pressure within its enclosed chamber. Consequently, the rubber sheet located within the chamber expands, achieving a specific angle between two separate finger joints. This process allows the joint to flex and move in a predetermined direction, facilitating the requisite motion of the robotic finger joint.

2.2 Manufacturing process

The manufacturing process of the robotic finger encompasses the assembly of a single-layer actuator, an EHD pump, and the injection of a conductive fluid. To construct the single-layer actuator, a copper sheet measuring 54 mm by 20 mm was attached to a PP sheet. Subsequently, any surplus copper sheet was removed using a cutting plotter, forming saw-tooth configured electrodes. The PP sheet was then disassembled utilizing a laser cutter. The same procedure was replicated for the VHB tape and the upper PP sheet. Subsequently, a rubber sheet and another PP sheet were affixed together using VHB tape, which constitutes

the structural vulnerability of the device. At the center of the PP sheet, a hole was created to serve as channels between pumps, and a thin PP sheet was attached to it using vinyl tape. Similar to the production process of EHD pump, this was manufactured using the aforementioned method, bonded together using VHB tape, and this process was repeated four times to generate multiple layers. The internal fluid employed in this process was 3M Novec 7300. A vacuum device was utilized to ensure the absence of any residual air within the assembly.

3 Mathematical model

We developed a physical model of the EHD pump-driven robotic finger, wherein both the EHD pump system and the finger dynamics were connected. All calculations and demonstrations were performed utilizing Mathematica 12.3, with symbolic computation techniques.

3.1 Rubber sheet deformation

The finger powered with a comb electrode acts as a pump that can manipulate a rubber sheet, causing the PP sheet to inflate like a balloon. This behavior is governed by a series of mathematical relationships and boundary conditions. The comb electrode structure in the EHD robotic finger is pivotal for electric field generation. We considered the rubber sheet as a circular disk supported at its periphery and subjected to a distributed load, representing stretching induced by working fluid pressure, as depicted in Fig. 2a. While the deflection $\delta_1(r)$ of the disk can typically be determined using infinitesimal deformation models, the applicability of the infinitesimal deformation model diminishes in cases where the out-of-plane deformation exceeds the thickness of the disk. Therefore, to avoid significant deflections, we resort to the energy method (Timoshenko and Woinowsky-Krieger, 1959) in our analysis, which takes into account the conservation of energy, wherein the deflection energy of the disk (U) is a composite of bending energy (U_1) and expanding energy (U_2), expressed as follows:

$$U_1=\frac{1}{2}\int_0^{2\pi}\int_0^a\left(M_r\frac{1}{R_1}+M_\theta\frac{1}{R_2}r\right)\mathrm{d}\theta\mathrm{d}r, \tag{1}$$

$$U_2=\frac{1}{2}\int_0^{2\pi}\int_0^a(N_r\varepsilon_r+N_\theta\varepsilon_\theta r)\,\mathrm{d}\theta\mathrm{d}r, \tag{2}$$

where M_r and M_θ represent the bending moments while R_1 and R_2 correspond to the curvature radii in the r and θ directions, respectively. N_r and N_θ denote the stresses and ε_r and ε_θ denote the strains of the middle surface in the r and θ directions, respectively. a is shown in Fig. 2a. By utilizing the relationships between bending moments M_r and M_θ and curvature radii R_1 and R_2, and when the bending rigidity $D=\dfrac{Et^3}{12(1-v^2)}$ (E is Young's modulus of the material and t is the thickness of the rubber sheet), U_1 can be expressed as follows (Koike and Hayakawa, 2021):

$$U_1=-\frac{D}{2}\int_0^{2\pi}\int_0^a\left[\left(\frac{1}{R_1}+\frac{v}{R_2}\right)\frac{1}{R_1}+\left(\frac{1}{R_1}+\frac{v}{R_2}\right)\frac{1}{R_1}\right]r\mathrm{d}r\mathrm{d}\theta, \tag{3}$$

where v represents Poisson's ratio of the material. We can express the curvatures R_1 and R_2 in terms of derivatives of the deflection δ_1 by leveraging geometric relationships, which can be formulated as

$$U_1=\pi D\int_0^a\left[\left(\frac{\mathrm{d}^2\delta_1}{\mathrm{d}r^2}\right)^2+\frac{1}{r^2}\left(\frac{\mathrm{d}\delta_1}{\mathrm{d}r}\right)^2+2v\frac{1}{r}\frac{\mathrm{d}\delta_1}{\mathrm{d}r}\frac{\mathrm{d}^2\delta_1}{\mathrm{d}r^2}\right]r\mathrm{d}r. \tag{4}$$

Then, U_2 can be formulated using the relationship between stresses N_r, N_θ and strains ε_r, ε_θ:

$$U_2=\frac{\pi tE}{1-v^2}\int_0^a\left[(\varepsilon_r+\varepsilon_\theta)^2-2(1-v)\,\varepsilon_r\varepsilon_\theta\right]r\mathrm{d}r. \tag{5}$$

Assuming a radial displacement denoted as $u(r)$, we can express ε_θ and ε_r in terms of $u(r)$:

$$\varepsilon_\theta=\frac{2\pi(r+u)-2\pi r}{2\pi r}=\frac{u}{r},$$
$$\varepsilon_r=\frac{\mathrm{d}u}{\mathrm{d}r}+\frac{1}{2}\left(\frac{\mathrm{d}\omega}{\mathrm{d}r}\right)^2, \tag{6}$$

where ω is the angular speed. Thus, by employing Eqs. (5) and (6), U_2 can be redefined as

$$U_2=\frac{\pi Et}{1-v^2}\int_0^a\left\{\frac{1}{4}\left(\frac{\partial\delta_1(r)}{\partial r}\right)^4+\frac{2vu}{r}\left[\frac{1}{2}\left(\frac{\partial\delta_1(r)}{\partial r}\right)^2+\frac{\partial u(r)}{\partial r}\right]+\left(\frac{\partial\delta_1(r)}{\partial r}\right)^2\frac{\partial u}{\partial r}+\left(\frac{\partial u}{\partial r}\right)^2+\left(\frac{u}{r}\right)^2\right\}r\mathrm{d}r. \tag{7}$$

Similar to the infinitesimal deformation model, the deflection of disk $\delta_1(r)$ can be expressed as follows:

$$\delta_1(r)=\delta_1(0)\left(1-\frac{r^2}{a^2}\right)^2\left(1-\frac{5+v}{1+v}\times\frac{r^2}{a^2}\right). \tag{8}$$

In this study, for a circumferentially supported disk subjected to a distributed load, the center and circumference should not deform in the radial direction. Under these boundary conditions, the radial displacement $u(r)$ can be expressed as follows:

$$u=c_0ar+(ac_1-c_0)r^2. \tag{9}$$

Here, c_0 and c_1 represent undetermined constants; we have considered the second-order term. The values of c_0 and c_1 can be determined by minimizing the strain energy U, leading to the following turning points:

$$\frac{\mathrm{d}U}{\mathrm{d}c_0}=0,\quad\frac{\mathrm{d}U}{\mathrm{d}c_1}=0. \tag{10}$$

The values of c_0 and c_1 can be calculated by integrating Eq. (10):

$$c_0=-1.189\frac{\delta_1(0)^2}{a^3},\qquad c_1=-0.537\frac{\delta_1(0)^2}{a^4}. \tag{11}$$

Assuming a Poisson's ratio of $v=0.5$, we can calculate U_1 and U_2 using the above values of c_0 and c_1:

$$U_1=5.386\pi\frac{Et^3\delta_1(0)^2}{a^2},\qquad U_2=0.947\pi\frac{Et\delta_1(0)^4}{a^2}. \tag{12}$$

The virtual work W caused by external force p can be computed as follows:

$$W=\int_0^{2\pi}\int_0^a p\,\delta_1(r)\,r\mathrm{d}r\mathrm{d}\theta=0.0278\pi a^2p\delta_1(0). \tag{13}$$

By employing Eqs. (12) and (13), we can derive the minimum deflection energy $U_{\min}$ as follows:

$$\frac{\partial(U_{\min}-W)}{\partial\delta_1(r)}=0. \tag{14}$$

Thus, we can obtain the following equation:

$$10.772\frac{Et^3}{a^2}\delta_1(0)+3.788\frac{Et}{a^2}\delta_1(0)^3=0.0278a^2p. \tag{15}$$

In cases where the deflection $\delta_1(0)$ significantly exceeds the thickness of the disk t, the first term becomes negligible. This approximation is equivalent to disregarding the bending energy U_1. Consequently, we can determine the maximum deflection $\delta_1(0)$ by solving Eq. (15), which yields the following result:

$$\delta_1(0)=0.133a\left(\frac{\pi pa}{Et}\right)^{\frac{1}{3}}. \tag{16}$$

3.2 Robotic finger geometry model

In this section, we consider the geometric relationship between the bending of the robot and the expansion of the rubber sheet. Referring to Fig. 2b, the actuation of the robotic finger can be simplified as a four-bar mechanism, where points A and B are fixed and the length of quadrilateral $ABDC$ remains constant. The distance between points A and D, denoted as "L", is equal to the maximum deflection of the rubber sheet, $\delta_1(0)$. In an EHD pump, the fluid pressure can be assumed as a power function or an exponential function of the applied voltage v (Mao et al., 2022b), given by:

$$p=a_1\mathrm{e}^{a_2v}, \tag{17}$$

where a_1 and a_2 are the fitting coefficients of the formula. Therefore, we can express $L(v)$ as:

$$L(v)=\delta_1(0)=0.133a\left(\frac{\pi pa}{Et}\right)^{\frac{1}{3}}. \tag{18}$$

Next, by applying the law of cosines, we can perform the following calculation:

$$\alpha(v)=\arccos\left(\frac{L_{AC}^2+L(v)^2-L_{CD}^2}{2L_{AC}\cdot L(v)}\right),$$
$$\beta(v)=\arccos\left(\frac{L_{AB}^2+L(v)^2-L_{BD}^2}{2L_{AB}\cdot L(v)}\right), \quad (19)$$

where the angle and length variables are shown in Fig. 2b. Finally, the angle between the robotic finger and the plane perpendicular to the horizon can be determined as:

$$\theta(v)=\pi-\alpha(v)-\beta(v)=\pi-\frac{0.23\left[L_{AB}^2-L_{BD}^2+4.708\left(e^{0.268v}\right)^{2/3}\right]}{\cos\left(L_{AB}\sqrt[3]{e^{0.268v}}\right)}-\frac{0.23\left[L_{AC}^2-L_{CD}^2+4.708\left(e^{0.268v}\right)^{2/3}\right]}{\cos\left(L_{AC}\sqrt[3]{e^{0.268v}}\right)}. \quad (20)$$

The above equation describes the deflection angle of the robotic finger in relation to various parameters and the expansion behavior of the rubber sheet. We can calculate the deflection angle of the flexed robotic finger compared to the initial position:

$$\Delta\theta(v)=\eta(\theta(v)-\theta_0), \quad (21)$$

where θ_0 represents the initial angle between the finger and the plane perpendicular to the horizon, and η represents the linear factor of this system, which is a constant. By applying Eqs. (20) and (21), the deflection angle can be deduced from the applied voltage.

4 Experimental results

In this study, we designed a robotic finger actuated by an EHD pump capable of bending 37° under the application of a voltage of 10 kV. We utilized high-definition video recorders to capture a detailed footage of the motion of the robotic finger, and conducted a meticulous analysis of joint angles for precise and accurate assessment. We measured the angles based on the geometric relationship between the bending of robotic finger limbs, employing video screenshots to accurately analyze and quantify the bending angles acquired in the experiments. Pressure readings were acquired through pressure sensors integrated into the system. The fabricated robot is depicted in Fig. 3a and the relation of pressure and applied voltage are shown in Fig. 3b. We introduced a mathematical model that correlates the applied voltage with the bending angle of the robot. The experimental data exhibited strong alignment with the predictions by the model, as confirmed through five repetitions, deflection measurements, and analysis of root mean square error (RMSE) values, which were 1.26, 2.28, 1.68, 0.99, and 3.16, respectively. Fig. 4a showcases a comparison between the actual robot bending and model simulation for the

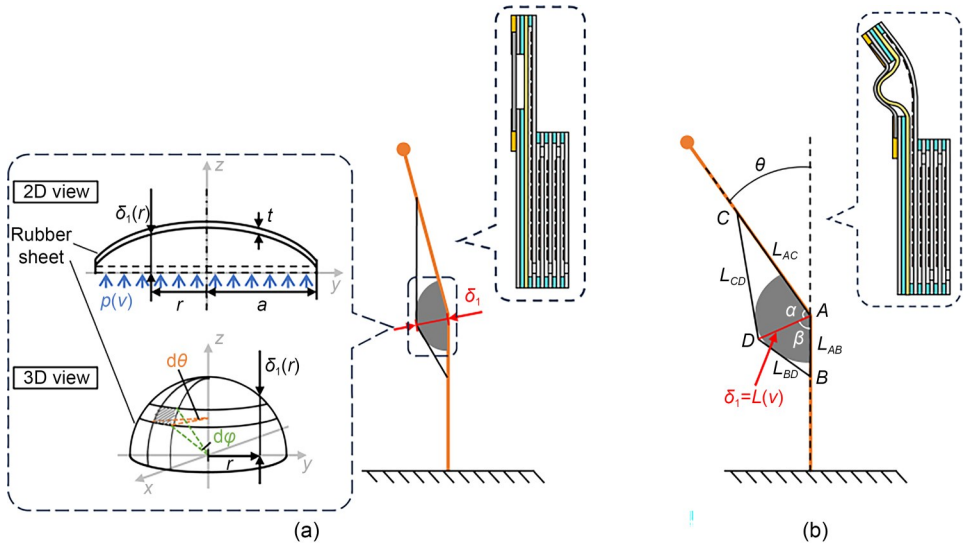

Fig. 2 Mathematical model parameters: (a) defined rubber sheet variables; (b) solving the bending angle of the robot from geometric dimensions

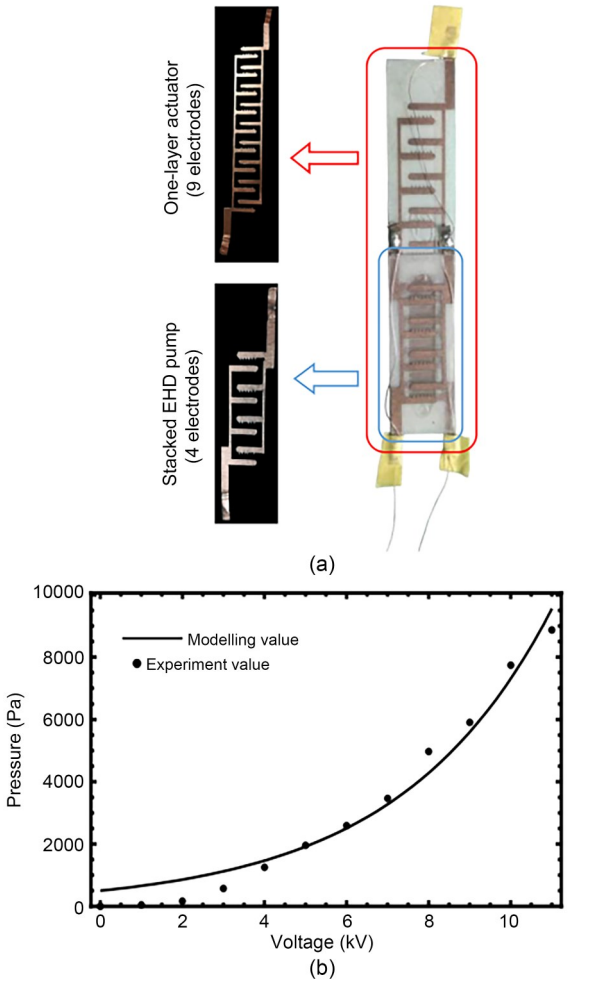

Fig. 3 Fabricated robotic finger: (a) structure of stacked EHD pumps; (b) generated pressure corresponding to the applied voltage

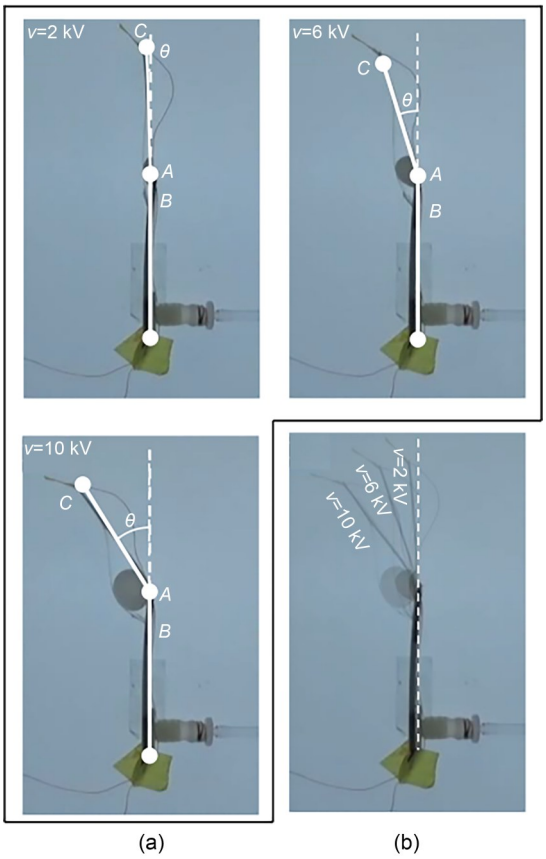

Fig. 4 Robot bending action: (a) simulated bending angle θ (marked using white line) and real robot bending; (b) real robot bending demonstration corresponding to the applied voltages of 2, 6, and 10 kV

applied voltages of 2, 6, and 10 kV. The results underscore the accuracy of our proposed mathematical model in describing the bending action of the robotic finger.

In addition, Fig. 4b provides a visual representation of the actual bending process of the robot. We utilized Eqs. (20) and (21) to compute the bending angle of the robotic finger for consecutively higher voltages (shown in Fig. 5a). A notable observation is the linear positive relationship between the applied voltage and the bending angle of the finger. This linearity arises because $\delta_1(0)$ is a power function of p with an exponent of 1/3, and p itself is an exponential function of v. This relationship results in the observed linear behavior between voltage and bending angle. The deflection of rubber sheet corresponding to the applied voltage is shown in Fig. 5b. The error percentages were calculated by comparing the actual and the predicted values. At voltage levels of 0, 2, 4, 8, and 10 kV, the error was consistently around 15%, indicating a relatively accurate prediction performance. It is noteworthy that, owing to the inherent simplification of certain parameters within the model, the outcomes produced by the model may exhibit certain deviations. Importantly, however, these discrepancies do not pose significant concern.

The relationship between the input voltage of EHD pump and the bending angle of the robotic finger, as described by our mathematical model, unveils an intricate interplay of EHD effects and mechanical dynamics. One of the principal findings of this research is the ability of the robotic finger to achieve a maximum bending angle of 37° under an input voltage of 10 kV. This bending motion, stimulated by the working fluid upon the application of voltage, exemplifies the functionality of the EHD pumps. Additionally, the constructed mathematical model not only underpins the

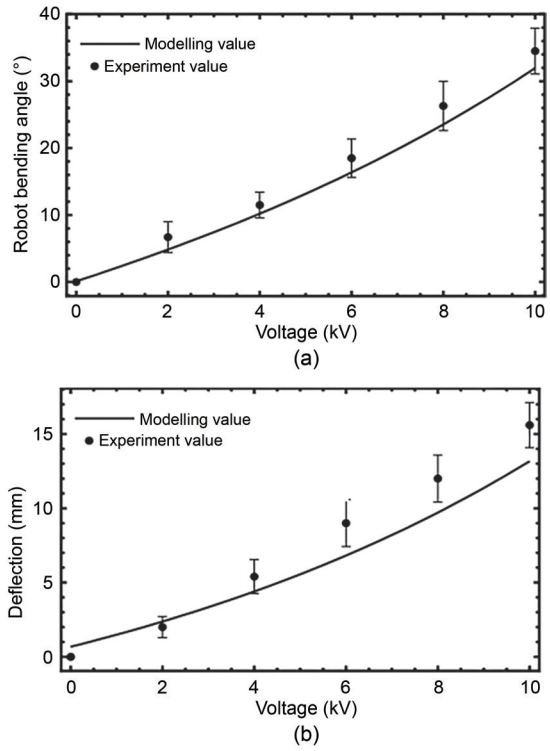

Fig. 5 Modeling results: (a) modeled vs. measured robot angle in the voltage ramp-up process; (b) modeled vs. measured deflection of rubber sheet

relationship between the EHD pump system and the finger dynamics but also corroborates the experimental results. While previous work (Mao et al., 2020b) predominantly emphasized modeling the power source process or focused on the advantages of EHD pump-driven actuators, our study delivers a comprehensive model that interconnects the entirety of the EHD driving system and the mechanical system of the robot. This holistic approach is of paramount significance for mapping other EHD pump-robot action systems and sets the stage for subsequent research.

While the present study has numerous merits, it is essential to note some of its limitations. First, the model initially presupposes a consistent Poisson's ratio with a constant value of 0.5 throughout the investigation and disregards potential fluctuations in this ratio across diverse materials or deformation conditions. Second, the model assumes a state of linear elastic behavior, excluding any nonlinear effects such as plasticity or viscoelasticity. Third, the assumption regarding a significant deflection that exceeds the disk thickness, though applicable to our study, might not hold for all soft robotic applications. Our model assumes constant material properties, overlooking material heterogeneity and potential changes. Additionally, it neglects heat generation from flow friction and dynamic force effects in a fluid-powered structure, introducing bias in the results. Constrained by inadequate pressure and power, the application of our model is limited to smaller robots or joints. For future research, we aim to combine multiple robotic fingers into a cohesive grasper. The holding force of this assembly will be assessed using tactile sensors, and we propose a thorough investigation of the object-holding capabilities of this grasper as well as the potential incorporation of sensory feedback mechanisms.

5 Conclusions

In summary, this work has pioneered the integration of an EHD robotic finger that incorporates a flexible rubber sheet embedded with soft EHD pumps. The model of this study links the electrical characteristics of the EHD pump (voltage input) with the geometric constraints of the robotic mechanism (deflection angle). The validity of this model has been empirically demonstrated. Our research findings primarily revolve around the manipulation of robotic arms and grasping mechanism. The synthesis of an experimental design and a comprehensive mathematical model showcases the potential of EHD pump-driven soft robotic applications ranging from delicate medical procedures to agile manufacturing processes. Moreover, the achieved maximum bending angle of 37° at 10 kV stands as a testament to the effectiveness of the proposed design and methodology. As an important foundation work in the realm of soft robotics, this research intends to serve as a catalyst for subsequent investigations in EHD pump-robot systems. Noteworthy examples include precision grasping in robotics, complex robotic hand operations, and promoting human-robot collaboration.

Author contributions

Xuehang BAI and Yanhong PENG processed the corresponding data and wrote the first draft of the manuscript. Dongze LI and Zhuochao LIU helped to organize the manuscript. Zebing MAO revised and edited the final version.

Conflict of interest

Xuehang BAI, Yanhong PENG, Dongze LI, Zhuochao LIU, and Zebing MAO declare that they have no conflict of interest.

References

Cacucciolo V, Shintake J, Kuwajima Y, et al., 2019. Stretchable pumps for soft machines. *Nature*, 572(7770):516-519. https://doi.org/10.1038/s41586-019-1479-6

Chen FY, Ren ZX, Lau GK, 2022. Maximal strengths of dielectric elastomer fingers for a passive grip. *Smart Materials and Structures*, 31(4):045014. https://doi.org/10.1088/1361-665X/ac57b0

Darabi J, Rada M, Ohadi M, et al., 2002. Design, fabrication, and testing of an electrohydrodynamic ion-drag micropump. *Journal of Microelectromechanical Systems*, 11(6):684-690. https://doi.org/10.1109/JMEMS.2002.805046

Funabora Y, 2018. Flexible fabric actuator realizing 3D movements like human body surface for wearable devices. IEEE/RSJ International Conference on Intelligent Robots and Systems (IROS), p.6992-6997.

Jiao ZD, Zhang C, Ruan JP, et al., 2021. Re-foldable origami-inspired bidirectional twisting of artificial muscles reproduces biological motion. *Cell Reports Physical Science*, 2(5):100407. https://doi.org/10.1016/j.xcrp.2021.100407

Kobayashi R, Nabae H, Endo G, et al., 2022. Soft tensegrity robot driven by thin artificial muscles for the exploration of unknown spatial configurations. *IEEE Robotics and Automation Letters*, 7(2):5349-5356. https://doi.org/10.1109/LRA.2022.3153700

Koike N, Hayakawa T, 2021. Evaluation of the deformation shape of a balloon-type dielectric elastomer actuator prestretched with water pressure. *ROBOMECH Journal*, 8(1):2. https://doi.org/10.1186/s40648-021-00189-2

Kong DQ, Hirata T, Li F, et al., 2024. A novel miniature swimmer propelled by 36° Y-cut lithium niobate acoustic propulsion system. *Sensors and Actuators A: Physical*, 365:114837. https://doi.org/10.1016/j.sna.2023.114837

Mao ZB, Yoshida K, Kim JW, 2019a. Developing O/O (oil-in-oil) droplet generators on a chip by using ECF (electro-conjugate fluid) micropumps. *Sensors and Actuators B: Chemical*, 296:126669. https://doi.org/10.1016/j.snb.2019.126669

Mao ZB, Yoshida K, Kim JW, 2019b. A droplet-generator-on-a-chip actuated by ECF (electro-conjugate fluid) micropumps. *Microfluidics and Nanofluidics*, 23(12):130. https://doi.org/10.1007/s10404-019-2298-7

Mao ZB, Yoshida K, Kim JW, 2019c. Fast packaging by a partially-crosslinked SU-8 adhesive tape for microfluidic sensors and actuators. *Sensors and Actuators A: Physical*, 289:77-86. https://doi.org/10.1016/j.sna.2019.02.020

Mao ZB, Yoshida K, Kim JW, 2020a. Active sorting of droplets by using an ECF (electro-conjugate fluid) micropump. *Sensors and Actuators A: Physical*, 303:111702. https://doi.org/10.1016/j.sna.2019.111702

Mao ZB, Nagaoka T, Yokota S, et al., 2020b. Soft fiber-reinforced bending finger with three chambers actuated by ECF (electro-conjugate fluid) pumps. *Sensors and Actuators A: Physical*, 310:112034. https://doi.org/10.1016/j.sna.2020.112034

Mao ZB, Iizuka T, Maeda S, 2021. Bidirectional electrohydrodynamic pump with high symmetrical performance and its application to a tube actuator. *Sensors and Actuators A: Physical*, 332:113168. https://doi.org/10.1016/j.sna.2021.113168

Mao ZB, Asai Y, Wiranata A, et al., 2022a. Eccentric actuator driven by stacked electrohydrodynamic pumps. *Journal of Zhejiang University-SCIENCE A (Applied Physics & Engineering)*, 23(4):329-334. https://doi.org/10.1631/jzus.A2100468

Mao ZB, Asai Y, Yamanoi A, et al., 2022b. Fluidic rolling robot using voltage-driven oscillating liquid. *Smart Materials and Structures*, 31(10):105006. https://doi.org/10.1088/1361-665X/ac895a

Mao ZB, Peng YH, Hu CL, et al., 2023. Soft computing-based predictive modeling of flexible electrohydrodynamic pumps. *Biomimetic Intelligence and Robotics*, 3(3):100114. https://doi.org/10.1016/j.birob.2023.100114

Nagaoka T, Mao ZB, Takemura K, et al., 2019. ECF (electro-conjugate fluid) finger with bidirectional motion and its application to a flexible hand. *Smart Materials and Structures*, 28(2):025032. https://doi.org/10.1088/1361-665X/aaf49a

Peng YH, Yamaguchi H, Funabora Y, et al., 2022. Modeling fabric-type actuator using point clouds by deep learning. *IEEE Access*, 10:94363-94375. https://doi.org/10.1109/ACCESS.2022.3204652

Peng YH, Sakai Y, Nakagawa K, et al., 2023a. Funabot-suit: a bio-inspired and McKibben muscle-actuated suit for natural kinesthetic perception. *Biomimetic Intelligence and Robotics*, 3(4):100127. https://doi.org/10.1016/j.birob.2023.100127

Peng YH, Li DZ, Yang XY, et al., 2023b. A review on electrohydrodynamic (EHD) pump. *Micromachines*, 14(2):321. https://doi.org/10.3390/mi14020321

Peng YH, Nabae H, Funabora Y, et al., 2024. Peristaltic transporting device inspired by large intestine structure. *Sensors and Actuators A: Physical*, 365:114840. https://doi.org/10.1016/j.sna.2023.114840

Shen YL, Chen MH, Skelton RE, 2023. Markov data-based reference tracking control to tensegrity morphing airfoils. *Engineering Structures*, 291:116430. https://doi.org/10.1016/j.engstruct.2023.116430

Smith M, Cacucciolo V, Shea H, 2023. Fiber pumps for wearable fluidic systems. *Science*, 379(6639):1327-1332. https://doi.org/10.1126/science.ade8654

Tan MWM, Bark H, Thangavel G, et al., 2022. Photothermal modulated dielectric elastomer actuator for resilient soft robots. *Nature Communications*, 13(1):6769. https://doi.org/10.1038/s41467-022-34301-w

Tawk C, Zhou H, Sariyildiz E, et al., 2021. Design, modeling, and control of a 3D printed monolithic soft robotic finger with embedded pneumatic sensing chambers. *IEEE/ASME Transactions on Mechatronics*, 26(2):876-887. https://doi.org/10.1109/TMECH.2020.3009365

Timoshenko S, Woinowsky-Krieger S, 1959. Theory of Plates and Shells. McGraw-Hill, New York, USA.

Zhang C, Chen JX, Li JT, et al., 2023. Large language models for human-robot interaction: a review. *Biomimetic Intelligence and Robotics*, 3(4):100131. https://doi.org/10.1016/j.birob.2023.100131